Cassini CIRS and ISS opposition effects of Saturn's rings -I. C ring narrow or broad surge?

E Déau, L. Dones, L. Spilker, A Flandes, Kevin Baillie, S Pilorz, M Showalter, M El Moutamid, J E Colwell

Cassini CIRS and ISS opposition effects of Saturn's rings – I. C ring narrow or broad surge?

E. Déau,[1,2]* L. Dones,[3] L. Spilker,[1] A. Flandes,[4] K. Baillié,[5] S. Pilorz,[6] M. Showalter,[6] M. El Moutamid[7] and J. E. Colwell[8]

[1]*NASA Jet Propulsion Laboratory, California Institute of Technology, Pasadena 91109 CA, USA*
[2]*Department of Earth and Space Sciences, UCLA, Los Angeles 90095 CA, USA*
[3]*SWRI, Southwest Research Institute, Boulder 80302 CO, USA*
[4]*Departamento de Ciencias Espaciales, Instituto de Geofísica, Universidad Nacional Autónoma de México, Coyoacán 04510, Mexico City, México*
[5]*IMCCE, Observatoire de Paris, Paris Sciences Lettres, CNRS, Sorbonne Universités, CNES, 75014 Paris, France*
[6]*SETI Institute, Carl Sagan Center, Mountain View, 94043 CA, USA*
[7]*Department of Astronomy, Center For Astrophysics and Planetary Sciences, Cornell University, Ithaca 14853 NY, USA*
[8]*Department of Physics, UCF, Orlando, 32816 FL, USA*

ABSTRACT

We focus on the thermal and optical opposition effects of Saturn's C ring seen by Cassini CIRS (Composite InfraRed Spectrometer) at 15.7 µm and ISS (Imaging Science Subsystem) at 0.6 µm. The opposition surge is a brightness peak observed at low phase angle ($\alpha \rightarrow 0°$). Saturn rings' opposition surge was recently observed in reflected light and thermal infrared emission by Cassini. There is debate on whether the C ring's thermal opposition surge width is narrow ($\lesssim 1°$) or broad ($\gtrsim 30°$). This surge is important because its width was used to define the scale of ring properties driving the thermal peak. We parametrize the CIRS and ISS phase curves with several morphological models to fit the surge shape. For five of the largest C ring's plateaus, we find that their thermal surge is 10 times wider than the optical surge and that the thermal surge width ($\sim 4°$) is neither narrow, nor broad. We compare radial differences between CIRS and ISS surge morphologies with the optical depth τ (from UVIS, UltraViolet Imaging Spectrograph) and water ice band depth (from VIMS, Visual and Infrared Mapping Spectrometer) profiles. We find that: water ice band depths (microscopic ring signatures) and τ (macroscopic ring signatures) show respectively little and large contrasts between the background and the plateaus. The thermal surge amplitude and τ are correlated, and we found no band depth dependence, contrary to the optical surge amplitude, which shows no correlation with τ. These correlations suggest a macroscopic scale dominance in controlling the C ring's thermal opposition effect.

Key words: planets and satellites: rings – planets and satellites: surfaces.

1 INTRODUCTION

A great deal can be learned about the nature of the ring particles and the regolith covering these particles' surfaces by modelling the changes in temperature, brightness, and colour with changing viewing geometry. In particular, studies using Cassini data demonstrated that these quantities exhibit considerable variations (Spilker et al. 2006; Altobelli et al. 2007, 2009; Porco et al. 2008; Bradley, Colwell & Esposito 2013; Déau et al. 2013a; Filacchione et al.

2014) when they are represented as a function of the phase angle α:

$$\cos \alpha = \sin B \sin B' + \cos B \cos B' \cos(\phi - \phi'), \qquad (1)$$

where B and B' are the spacecraft and solar elevation angles with respect to the ring plane, ϕ is the observer longitude ($0° \leq \phi \leq 360°$), and ϕ' is the longitude of the Sun's direction.

This paper focuses on the optical and thermal photometric behaviours of Saturn's rings via the opposition effect (or brightening), which is a special viewing geometry that allows studies of the ring brightness when α decreases to almost zero degrees (in fact, owing

* E-mail: deau@jpl.nasa.gov

to the finite angular size of the Sun, a phase angle of zero degrees is not observable at Saturn's heliocentric distance, see Déau 2012).

The ring opposition effect observed at visible wavelengths (or optical opposition effect) has a shape that can be quantified by two morphological features. First, a non-linear increase in the intensity occurring when α decreases from 6° to $\sim$0°.03 (Lumme & Irvine 1976; Poulet et al. 2002). Second, a linear increase in the intensity when α decreases from 30° to 5° (Déau et al. 2013a). These two behaviours were modelled by a logarithmic function of the phase angle for both data at optical and thermal infrared (IR) wavelengths (Altobelli et al. 2007; Déau 2007). Previously, the bulk of the information on the optical opposition effect of Saturn's rings was provided by Earth-based data (Poulet et al. 2002; French et al. 2007; Salo & French 2010). In particular, French et al. (2007) observed the 'true' opposition (from 6° all the way down to the solar angular radius) quite well. Cassini imaging data have since complemented the phase angle coverage of Earth-based data, first: at phase angles smaller than the angular radius (where the phase curve flattens, Déau 2012), and second: at phase angles greater than 6° up to 180° in the forward scattering direction, e.g. Déau (2007) and Hedman & Stark (2015).

The ring thermal opposition effect is, strictly speaking, the increase of temperature (or IR brightness) when the phase angle decreases down to $\sim$0°.03. However, there is still a debate on whether or not the ring thermal surge is narrow (less than a degree) or broad (several tens of degrees), see Wallis et al. (2005, 2006) and Altobelli et al. (2007, 2009). This is particularly important because the thermal surge width was used in Altobelli et al. (2007, 2009) to derive ring properties.

Another puzzling result from previous thermal opposition effect studies is the zero phase temperature differences between two close high-τ regions in the C ring (plateaus # 1 and 2), see Altobelli et al. (2007). Indeed, these two regions have nearly the same optical depth, but their effective temperatures at zero phase are very different (Altobelli et al. 2007, fig. 12), which is difficult to understand, considering that the values of albedo, and band depth are very similar in these two regions (Cooke 1991; Déau 2007; Hedman et al. 2013).

The goal of this paper is to develop a better understanding of microscopic and macroscopic properties of the ring particles from a novel study combining visible and thermal opposition effect data. However, to achieve this goal, there are several major issues to overcome that are related to the fact that the opposition effect in optical and IR wavelengths is still poorly understood. So far, there is a limited, but accurate knowledge of some microscopic and macroscopic signatures of the rings from the data taken by various instruments onboard Cassini. The ring optical depth obtained by stellar occultations is a pure macroscopic signature of the ring layer, since its variations contain information that allows retrieval of the size distribution of the ring particles (Zebker, Marouf & Tyler 1985; Jerousek et al. 2016), the clumpiness of the rings (Colwell, Esposito & Sremčević 2006; Colwell et al. 2007, 2009a; Hedman et al. 2007), and the surface density of the ring layer (Baillié et al. 2011; Colwell et al. 2009a,b). On the other hand, during the last few years, additional constraints have been derived from the water ice band depths in the near-IR (Nicholson et al. 2008; Filacchione et al. 2012; Hedman et al. 2013). These water ice absorption bands are at 1.25, 1.5, 2.0, 3.0, and 4.5 µm. The ring spectra also show steep slopes at wavelengths below 0.6 µm, which cannot be attributed to water ice. Hedman et al. (2013) showed that these slopes are related to a contaminant that preferentially absorbs at short visible and near-ultraviolet (UV) wavelengths.

This contaminant could either be nanometre-sized grains of iron, haematite, or organic compounds (Cuzzi et al. 2009). Comparisons between surge morphology and spectral properties have been done in the past for laboratory samples (Déau, Spilker & Flandes 2016), and they show interesting correlations, which imply the role of the sample grain microstructure. Therefore, we will use water ice band depths jointly with spectral slopes in the UV as a reference for microscopic signatures due to the ring regolith, see Appendix A. We will compare the results of optical and thermal surge morphology to the τ-related properties, and to the water ice band depths and the UV spectral slopes of the rings related to regolith properties.

Comparing thermal and optical surges using CIRS (Composite InfraRed Spectrometer) and ISS (Imaging Science Subsystem) data is not trivial because both data sets discriminate different quantities. The ISS data are brightness normalized to the solar flux (*I/F*), while CIRS data can be either IR brightness (I_k, where $k = 1/\lambda$ is the wavenumber, and λ the wavelength, the solar flux is negligible in thermal IR, see Fig. 5) or effective temperatures (*T*), see Appendix B3. For this reason, we will use brightness quantities for both instruments. We will use only morphological models in this paper. To explain the narrow/broad surge, we will use various types of morphological models to fit the optical and thermal opposition surge, because most morphological models are dependent on the phase angle coverage and the phase angle sampling, see Déau (2007) and Déau, Flandes & Spilker (2013b), and the ISS and CIRS data sets have different phase angle coverage and sampling. However, for our main trends, we will use the same morphological model to fit both optical and thermal opposition data.

In this paper, we will focus on the same C ring regions studied by Altobelli et al. (2007) – see Table A1, because these regions mix low-τ and high-τ regions (Fig. A1) and show distinct variations of microscopic and macroscopic properties with radial distance to Saturn. Indeed, the variations of regolith properties inferred by water ice band depths are monotonic, (Filacchione et al. 2012; Hedman et al. 2013), while the ring layer properties are related to τ and vary abruptly with radial distance (Colwell et al. 2009a; Baillié et al. 2011). This means that our approach will not refer to the opposition effect mechanisms that are usually used to constrain the ring layer and the regolith. Indeed, since there is still a debate on whether or not the ring thermal surge is narrow or broad, using opposition effect models is premature at this point. In this paper, we plan to:

(1) quantify the angular width of the C ring's narrow thermal opposition surge found by Altobelli et al. (2007);

(2) determine whether the C ring's thermal opposition surge is narrow (Altobelli et al. 2007) or broad (several tens of degrees, Altobelli et al. 2009);

(3) confirm whether or not plateaus 1 and 2 of Altobelli et al. (2007) are different in terms of thermal surge;

(4) if yes, explain these differences in terms of microscopic and/or macroscopic properties;

(5) determine the scale of the ring properties responsible for the C ring's optical and thermal opposition surges.

In Section 2, we present the data sets used here, including Cassini data on the optical and thermal opposition surge of Saturn's rings as well as the morphological parameters retrieved from the phase curves using morphological models. The results are presented in Section 3. We interpret the results in Section 4, and we give the main conclusions in Section 5. In the second installment of this article series, the optical and thermal opposition effect's widths will be interpreted in terms of opposition effect mechanisms.

2 DATA COLLECTION, DESCRIPTION, PROCESSING, AND MORPHOLOGICAL MODELLING

2.1 Optical opposition effect from ISS data

Cassini's ISS instrument consists of two cameras, a wide-angle camera (WAC) and a narrow angle camera (NAC), both equipped with 1024×1024 CCD pixels (Porco et al. 2004). Using ISS images like those shown in Fig. 1, it can be seen that the overall look of the C ring is dominated by confined bright features called plateaus, superimposed on a faint, gently undulating structure called the background. As noted by Colwell et al. (2009a), a comparison between images and optical depth profiles (Fig. A1) reveals that almost all these brightness variations actually reflect variations in optical depth in this ring. As we wish to explain some of the discrepancies found by Altobelli et al. (2007), we propose to use the ring regions used in their study, which consists of five of the C ring outer plateaus and one narrow region of the C ring background. The plateau regions are highlighted in Fig. 1 and their references are given in Table 1.

We have used our previous work (Déau et al. 2013a) on the ISS images to retrieve the optical phase curves of the C ring plateaus and background. In the ISS images from which the opposition phase curves were extracted, see Déau et al. (2013a, table 2), the opposition spot is visible (see e.g. the C/B ring boundary in Fig. 1, left), because the phase angle varies from almost zero to $2°$ in a single image. Seeing the opposition spot is pretty unique. Indeed, with Earth-based observations, the Earth-Saturn distance makes α nearly constant over the rings. Therefore, to obtain phase curves, observations at different distances (or epochs) have to be combined, e.g. French et al. (2007, fig. 1). This is why ring images from Earth do not exhibit the opposition spot. As explained in Introduction, the opposition effect can be characterized by means of morphological parameters. The surge is described by an amplitude and a width (particularly a half-width at half-maximum, HWHM), while the linear part is described by a slope (Kaasalainen, Muinonen & Piironen 2001).

No detail will be made on the colour variations of the opposition surge, as we focus on the results from the CLEAR filter NAC and WAC images (central wavelengths of 0.611 and 0.635 μm, respectively).[1]

We use two morphological models in the following: to characterize the overall shape of the optical surge, we use the logarithmic model of Bobrov (1970) and to derive the morphological parameters of the surge, we use the linear model of Lumme & Irvine (1976). First, we have fit the ISS data in *I/F* by the logarithmic model of Bobrov (1970):

$$I/F = a_0 + a_1 \ln \alpha, \tag{2}$$

and have presented the results of these fits along with the data on the left-hand panels of Fig. 2. This representation allows us to see that the ISS data in *I/F* roughly conform to a line when the *x*-axis is in logarithmic scale. This latter point will be important for our comparison with the CIRS data in the next section.

---

[1]Each camera has two filter wheels, with 12 filters on each wheel on the NAC and nine filters on each wheel on the WAC. The spectral range for the NAC is from the UV to the near-IR (200–1050 nm), while the WAC only operates at visual and near-IR wavelengths (380–1050 nm), see also Porco et al. (2004, table VIII) and Déau et al. (2013a, table 1).

In this paper, we compare ISS data to CIRS data. While we use the exact same observation containing the opposition spot (the observation 0PHASE001 during Rev 10) for both ISS and CIRS, comparing reflected brightness to mid- or far-IR data is not straightforward. In the ISS data set of Déau et al. (2013a), the phase curve data, originally in *I/F*, were converted to $\varpi_0 P(\alpha)$ using the Chandrasekhar (1960) formula to account for the variation of viewing geometries from one image to another and within a single image. ϖ_0 is the single scattering albedo and $P(\alpha)$ is the single scattering phase function, as the model assumes single scattering. However, $\varpi_0 P(\alpha)$ is not exactly a brightness, and comparison with CIRS data could potentially be difficult to interpret. This is why we have used the ISS data set of Déau et al. (2013a) in *I/F*.

For the morphology of the optical surge, we used our previous results with the linear model of Lumme & Irvine (1976). On the right-hand panel of Fig. 2, the amplitude and angular width values of Déau et al. (2013a) from the linear model are given for the six regions of interest (ROIs) studied by Altobelli et al. (2007). Then, we have derived the morphological parameters of the surge using the linear model of Lumme & Irvine (1976) with $\alpha_1 = 0°3$ and $\alpha_2 = 1°5$:

$$I/F(\alpha < \alpha_1) = -A_0 \cdot \alpha + B_0, \tag{3}$$

$$I/F(\alpha > \alpha_2) = -A_1 \cdot \alpha + B_1. \tag{4}$$

Then, the output parameters of the linear fit allow the derivation of the morphological parameters of the surge:

$$A = \frac{B_0}{B_1} \text{ and HWHM} = \frac{(B_0 - B_1)}{2(A_0 - A_1)}. \tag{5}$$

The amplitude A is dimensionless. HWHM is given in degrees. To estimate the error bars, we use the propagation of errors method of Déau et al. (2013b). For the linear-by-parts model, we obtain:

$$\Delta A = \left[\left(\frac{\Delta B_0}{B_1} \right)^2 + \left(\frac{B_0}{B_1^2} \times \Delta B_1 \right)^2 \right]^{1/2} \tag{6}$$

$$\Delta \text{HWHM} = \left[\left(\frac{\Delta B_0}{2(A_0 - A_1)} \right)^2 + \left(\frac{\Delta B_1}{2(A_0 - A_1)} \right)^2 \right.$$
$$\left. + \left(\frac{(B_0 - B_1)}{2(A_0 - A_1)^2} \right)^2 \left(-(\Delta A_0)^2 + (\Delta A_1)^2 \right) \right]^{1/2} \tag{7}$$

where ΔA_0, ΔA_1, ΔB_0, and ΔB_1 are the 1σ uncertainty estimates. We have found that $\Delta A \sim 0.01$ and $\Delta \text{HWHM} \sim 0°02$ for the background and the plateaus.

The values of A and HWHM are reported in Fig. 2.

To enhance the ISS opposition effect data set description, we propose to compare our results with those of Déau et al. (2013a) with the ISS data in $\varpi_0 P(\alpha)$. Indeed, as explained previously, we have used the ISS data in *I/F* instead of $\varpi_0 P(\alpha)$. This was primarily because $\varpi_0 P(\alpha)$ is not exactly a brightness. There is also a second reason. As the Chandrasekhar (1960) conversion uses the optical depth, it might result in an optical depth dependence of the $\varpi_0 P(\alpha)$ phase curves, and in the morphological parameters. By comparing the amplitude values from Table 2, we do note a slight discrepancy of 0.1 between the values from *I/F* data and the ones from the $\varpi_0 P(\alpha)$, but we do not find any changes in the variations of A with distance to Saturn. This indicates that the Chandrasekhar (1960) inversion
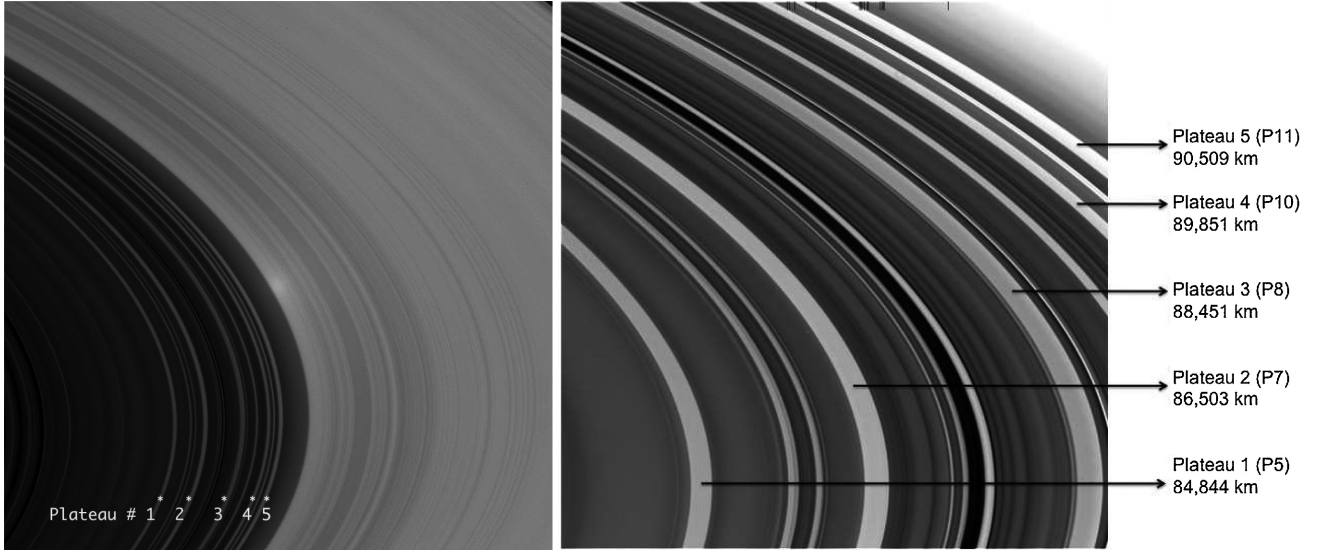
Figure 1. From left to right: ISS images W1498452080 (from the observation 0PHASE001 during Rev 10) and N1477742794 (from the observation COMPHILIT001 during Rev A). The phase angle is $1°25 \pm 1°25$ for the WAC image and $144° \pm 0°8$ for the NAC image. Both images were taken with the CLEAR filters. The plateaus studied here are labelled using the nomenclature of Altobelli et al. (2007) and Colwell et al. (2009a). The radial distance given in the left-hand image represents the distance at the centre of the feature.

Table 1. Summary of the six ROIs' characteristics (original and alternate names, and boundaries R_{min} and R_{max}).

Region name (Altobelli et al. 2007)	Alternate name (Colwell et al. 2009a)	R_{min} (km)	R_{max} (km)
Plateau 1	P5	84 750	84 950
Plateau 2	P7	86 375	86 605
Plateau 3	P8	88 350	88 595
Plateau 4	P10	89 790	89 940
Plateau 5	P11	90 405	90 610
Background	–	82 800	83 100

did not affect the surge amplitude parametrization. For the angular width of the surge, we note that the variations with radial distance are different from the two methods. To explain this, we have to explain how the phase curves of Déau et al. (2013a) were built.

The ISS data set of Déau et al. (2013a) consists in phase curves of individual and non-overlapping regions called ring features. The data of a specific ring feature are extracted in a range of radial distances to Saturn. This method allows the signal extraction for the same feature in multiple images, creating a large ensemble of points for each phase curve (more than 10 000). A large number of these points have the same phase angle, but slightly different illumination geometry, see fig. 1 of Déau (2015). This results in the thickness of the phase curves of Déau et al. (2013a). The phase curve thickness when the data are in I/F or $\varpi_0 P(\alpha)$ does not affect A (since both data sets cover the smallest phase angles). However, this difference can definitely affect HWHM, because the thickness of the phase curves affects the determination of the surge width. Because the Chandrasekhar (1960) inversion tends to correct for geometry effects, which is the origin of the thickness of the ISS data, the I/F phase curves are thicker than the $\varpi_0 P(\alpha)$ curves. As a result, we believe that HWHM variations between the plateaus in I/F are less reliable than those of A.

2.2 Thermal opposition effect from CIRS data

The CIRS instrument is a Fourier transform spectrometer, and a dual interferometer that operates with an improved spectral and spatial resolutions (relative to Voyager) at wavelengths that range from 7 to $1400 \mu m$ ($7-1500 cm^{-1}$) covering a broader window from the near-IR up to the sub-millimetre range (Flasar et al. 2004). CIRS is composed of two sensing instruments: a Martin–Puplett polarization interferometer with a far-IR focal plane FP1, operating between 17 and $1400 \mu m$ (a 4.3 mrad circular monopixel), and a conventional Michelson interferometer with two focal plane arrays: the mid-IR focal plane FP3 operating between 9 and $17 \mu m$ (an array of 0.273 mrad of 1×10 pixels), and the near-to-mid-IR focal plane FP4 operating between 7 and $10 \mu m$ (an array of 0.273 mrad of 1×10 squared pixels).

For the opposition effect data, we use four CIRS observations that contain the smallest phase angles in the specific range of solar elevation we selected. These scans were used by Altobelli et al. (2007) in their narrow thermal surge study. We will call them the 'four originals'. Our version of these scans were processed by Pilorz on 2012 May 08. Scan g, an additional scan absent from the study of Altobelli et al. (2007) but used by Morishima et al. (2017) as scan H1, is added, and was processed by Pilorz on 2016 February 01. The viewing geometries are given in Table 3 and shown in Fig. 3.

Some viewing geometry parameters such as the local time and the solar elevation impact the ring thermal phase curves (Leyrat et al. 2008; Flandes et al. 2010). One advantage of the four original scans is the proximity of their data acquisition, which insures a similar solar elevation geometry (see values of B' in Table 3). Also, all the scans were taken in the afternoon (see Fig. 3), thus minimizing local time effects.

As an example, the CIRS spectra of scan a (CIRS_010RI_ 0PHASE001_VIMS), is given in Fig. 4 for the C ring. It is actually a spectrogram, meaning the wavelength is given along the y-axis, while the radial distance to Saturn is plotted on the x-axis. The IR brightness represented in Fig. 4 is colour coded. To better highlight
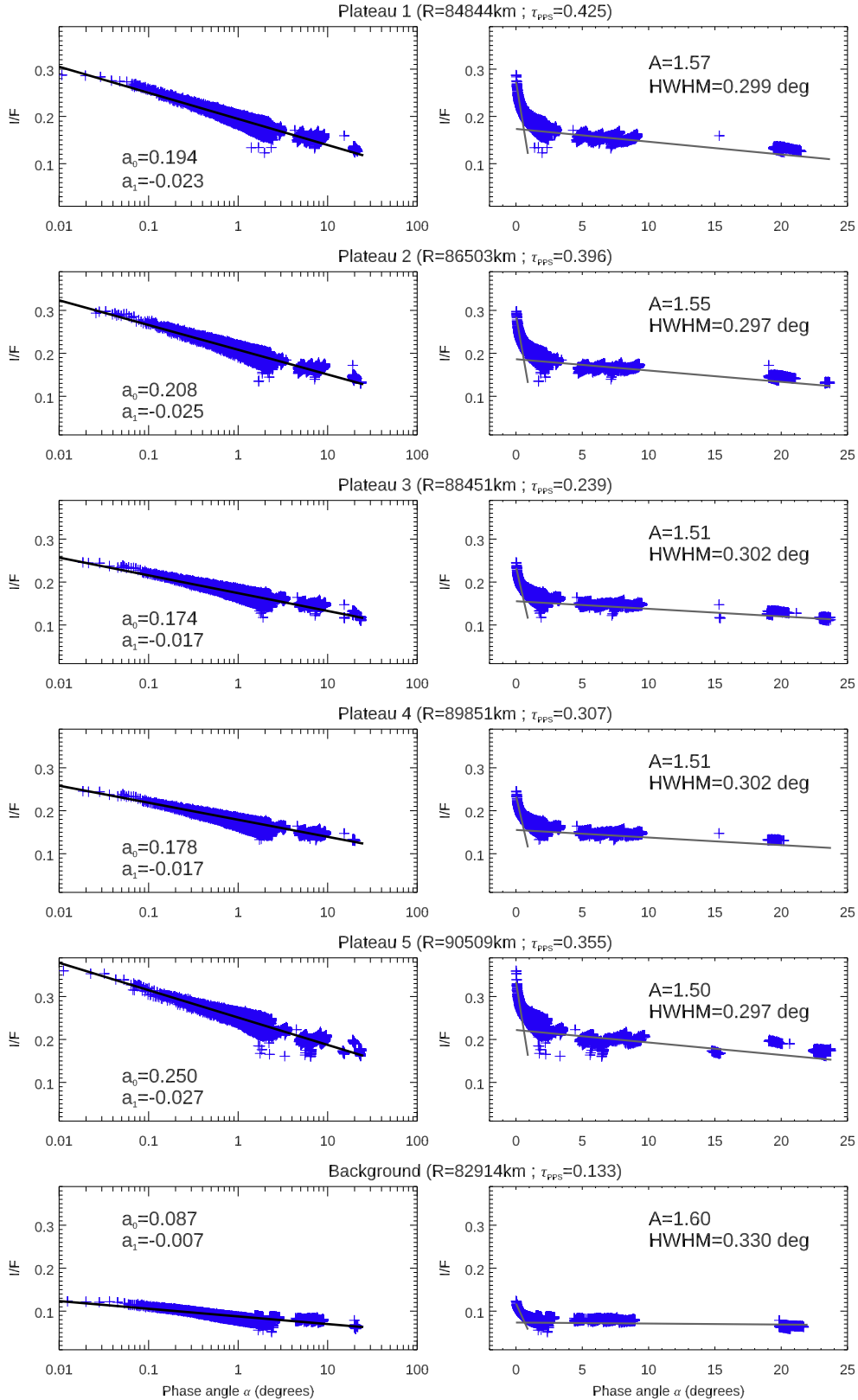
Figure 2. ISS optical brightness *I/F* versus phase angle α derived for the plateaus numbered consistently with Fig. 1 and for the C ring's background. On the left-hand panels, the data points have been fit by a logarithmic function (solid curve), and the parameters a_0 and a_1 are obtained with the logarithmic model with equation (2). On the right-hand panels, the morphological parameters of the surge are derived from the linear model seen in equations (3) and (4), whose functions are plotted as grey thin lines. The ISS data are retrieved from the study of Déau et al. (2013a) and the morphological parameters of the surge are obtained from equation (5). Note that the scale of the *y*-axis has been kept constant to judge the brightness level of a region with respect to the other. Voyager PPS optical depth values are from Déau et al. (2013a), and will be used as a reference from now on.

Table 2. Summary of the morphological parametrization of the optical surge for the six ROIs.

Phase curve unit	I/F		$\varpi_0 P(\alpha)$	
Reference	This study		Déau et al. ([2013a](#))	
Morph. param.	A	HWHM	A	HWHM
Background	1.60	0°330	1.52	0°310
Plateau 1 (P5)	1.57	0°299	1.49	0°270
Plateau 2 (P7)	1.55	0°297	1.45	0°267
Plateau 3 (P8)	1.51	0°302	1.40	0°261
Plateau 4 (P10)	1.51	0°302	1.40	0°290
Plateau 5 (P11)	1.50	0°297	1.39	0°254

the brightness in each focal plane, the same colours are used for each range of brightness, see ranges for FP1, FP3, and FP4 in Fig. [4](#).

FP1, FP3, and FP4 data together can potentially bring an unprecedented combination of spatial and spectral information. However, these data can be hard to interpret because of the differences in the technical properties of each spectrometer [i.e. the field of view (FOV), the pixel size, and the sensitivity].

First, the angular size of the FOV is different for the three focal planes, resulting in a different radial resolution and phase angle range of each pixel. For example, for scan a that was taken at 7.8 R_Y, the radial resolution is between 1611.8 and 4424.1 km pixel^{-1} for FP1, and 164.4–238.5 km pixel^{-1} for FP3 and FP4, whereas for scan d (taken at 21.9 R_Y), the radial resolution is between 5071 and 10 141 km pixel^{-1} for FP1, and 415.3–930.4 km pixel^{-1} for FP3 and FP4. This actually means that FP1 does not resolve any plateau region[2] for the observations selected (another evidence is also given in Fig. B9 of Appendix B3 with the behaviour of the scaling factor β), and averages the signal with the surrounding background in each footprint. This explains why FP1's spectrogram does not look like FP3's spectrogram (Fig. [4](#)), and the discrepancy in the IR brightnesses of the FP1 and FP3 spectra (see Fig. [5](#)). We note that there is no discrepancy in the background region plotted in the lower right panel of Fig. [5](#), where FP1 and FP3 spectra overlap perfectly. This means that FP1 successfully resolved the background.

Other than the pixel size, the boresight can also intervene. Indeed, FP1, FP3, and FP4's boresights are not exactly co-aligned, meaning that the pixels of each spectrometer do not cover exactly the same phase angles. For example, for scan a, FP1 is not aligned with the opposition spot's centre by ∼0°2, and a single FP1 pixel covers about 0°4; while FP3's and FP4's 10 pixels cover in total ∼0°06, with the central pixel aligned with the spot's centre (with the smallest phase angle of ∼0°07). Here again, the agreements and disagreements between FP3 and FP1 seen in Fig. [5](#) are very meaningful. For the plateaus, the disagreement indicates that FP1 does not resolve the opposition peak seen by FP3, while the agreement between FP3 and FP1 for the background implies that there is no narrow surge.

Finally, the sensitivity of the three focal planes is different. To quantify CIRS's sensitivity, we use the NESR (Noise Equivalent Spectral Radiance), which corresponds to the signal for which the signal-to-noise ratio is unity. The NESR depends on the spectral

resolution (from 0.5 to 20 cm^{-1}), which is controlled by the scan time, set in units of 1/8 s (= 1 RTI or Real Time Interrupt), corresponding to the time (from 2 to 52 s) the mechanism takes to travel the maximum mirror distance of 1.04 cm. For scan a (Fig. [4](#)), RTI = 38, which gives a spectral resolution of 16.50 cm^{-1} ([3]) with the fitting function:

$$\Delta k = c_0 + \frac{c_1}{\text{RTI}} + \frac{c_2}{\text{RTI}^2} + \frac{c_3}{\text{RTI}^3} \qquad (8)$$

where $c_0 = 0.7693$, $c_1 = 554.274$, $c_2 = -34540.1$, and $c_3 = 1.45999.10^6$ ([4]).

The NESR is unfortunately not available for a spectral resolution of 16.50 cm^{-1} ([5]), but a lower spectral resolution corresponds to a larger sensitivity, since the NESR is roughly inversely proportional to Δk (Flasar et al. [2004](#), fig. 29). Values of NESR per minute integration for a spectral resolution of 15.67 cm^{-1} (which are available) should correspond to the upper limit of NESR for scan a: 3×10^{-10}–7×10^{-9} W cm^{-2} sr^{-1} cm^{-1} min^{-1} for FP1, 8×10^{-10}–7×10^{-9} W cm^{-2} sr^{-1} cm^{-1} min^{-1} for FP3, and 1.5×10^{-10}–3×10^{-10} W cm^{-2} sr^{-1} cm^{-1} min^{-1} for FP4, see Flasar et al. ([2004](#), fig. 29). As a result, the sensitivity of scan a can be considered as good for most FP1 and FP3 spectra. It is not the case for FP4, whose level is below the NESR. It is particularly interesting to insist on that fact because FP4 wavenumbers should encompass the crossing between the tail of the emitted *Planck* function and reflected solar *Planck* function (Fig. [5](#)). Considering the NESR implies that FP4 data for this observation are not exploitable for the C ring.

Therefore, the signal received is very noisy in FP4 (Fig. [4](#)), a little bit noisy in FP3, and not noisy in FP1, except at the edges of the spectral range covered by FP1 (see Fig. [5](#)).[6] The edges are exactly where it would be interesting to compare the signal from the three focal planes. This is what we have done in Fig. [5](#) (the extreme edges have been removed), and the overlap is correct with FP3 and FP4, but not with FP1, which could be explained by the different pixel size and boresight of FP3 and FP1. As a result, the information about the plateaus contained in FP1 is not only contaminated by the surrounding background, but biased by the large FOV of FP1's footprint. Therefore, we focus on FP3 to derive the thermal opposition phase curves in the following.

Contrary to Altobelli et al. ([2007](#)), who derived temperatures from FP3 data, we derive the phase curves in IR brightness (or spectral radiance to be accurate). This allows us to avoid any complications of the retrieval of the effective temperature from the FP3 spectra not encompassing the wavelength of the *Planck* function's peak, see discussion in Altobelli et al. ([2007](#)). Moreover, as stated in Introduction, this will insure a coherent comparison with

---

[2]This issue could have been avoided with a smaller distance of the spacecraft to the rings. Indeed, to spatially resolve the plateaus with FP1, the spacecraft has to be, at most, at a distance of 0.49 R_Y from the target (as during the Saturn Orbit Insertion). However, in the *four original* observations, the spacecraft distance is about 8–22 R_Y, see Table [3](#).

[3]Note that a spectral resolution of 16.50 cm^{-1} is considered as a low spectral resolution (Flasar et al. [2004](#)), because the lowest wavenumbers (the tail of the *Planck* function at 50–100 cm^{-1}) would not be well sampled with FP1. However, this spectral resolution is correct for FP3 and FP4, since they cover large range of the longest wavenumbers (respectively, 600–1100 and 1000–1500 cm^{-1}).
[4]See http://pds-rings.seti.org/volumes/COCIRS_0xxx/ COCIRS_0201/DOCUMENT/DATASIS.PDF
[5]The only NESRs available are for spectral resolution of: 0.53, 1.00, 2.85, 6.60, and 15.67 cm^{-1}.
[6]Note that our FP4, FP3, and FP1 spectral data still contain RTI interference noise. The interferogram despiking method described by Carlson et al. ([2009](#)) has not been applied here. For more details, see also 'Interferences on CIRS interferograms and spectra: a user guide' by Conor A. Nixon and colleagues at http://pds-rings.seti.org/volumes/COCIRS_0xxx/COCIRS_0 201/DOCUMENT/cirs_interferences.pdf

Table 3. Summary of the relevant technical, geometrical, and spectral characteristics for the *four original* scans used in this work. α, B, and B' are defined in equation (1). The distance between Cassini and the CIRS footprint on the rings is given in Saturn radii (R_Y) and the distance from Saturn to the Sun is given in astronomical units. Δk is the spectral resolution in cm^{-1}. RTI is a measure of the spectral resolution. An additional scan (aka scan g) used by Morishima, Turner & Spilker (2017) is added.

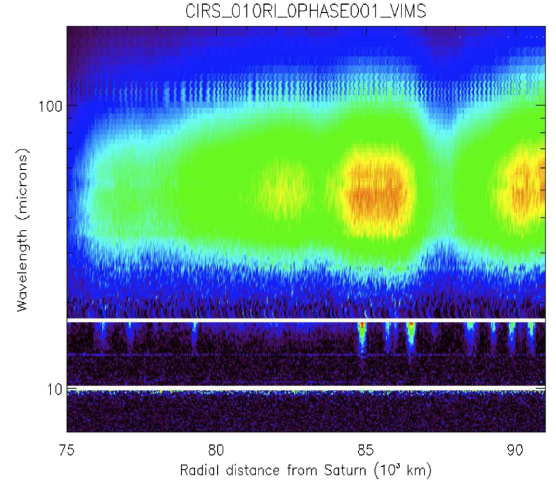| Observation	Observation name	Start date	α	$\|B\|$ range	B'	Distance (R_Y)	Distance (au)	Δk (cm^{-1})	RTI
Scan a	CIRS_010RI_0PHASE001_VIMS	2005-177T03:15:45	0°.07–3°.75	17°.4–21°.5	−21°.2	7.8	9.078	16.50	38
Scan b	CIRS_008RI_SUBML20LP001_PRIME	2005-140T11:28:15	0°.3–9°.5	20°.7–22°.1	−21°.6	9.0	9.073	1.15	224
Scan c	CIRS_007RI_TEMPL20LP001_PRIME	2005-122T04:01:05	14°.7	18°.7–22°.3	−21°.8	11.9	9.071	16.50	38
Scan d	CIRS_009RI_SUBML20LP001_PRIME	2005-157T03:00:35	36°.5	20°.0–21°.1	−21°.4	21.9	9.076	1.15	224
Scan g	CIRS_006RI_SUBML07LP001_PRIME	2005-104T06:53:41	27°.9	7°.6–7°.7	−22°.0	9.9	9.069	1.15	224
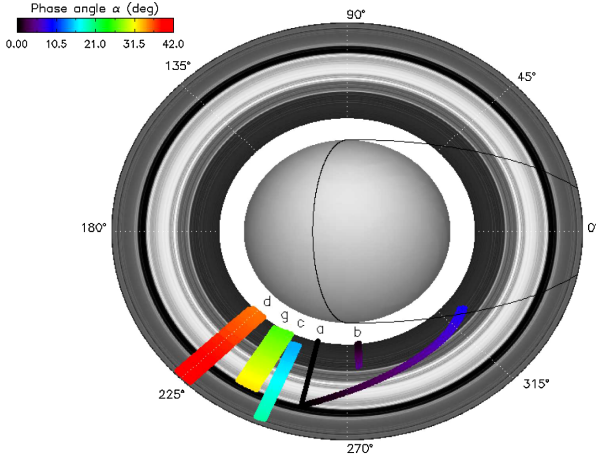
Figure 3. Polar view of Saturn's rings showing the *four original* scans and scan g. The CIRS footprints are colour coded by phase angle. The rings appears as concentric circles in a grey scale proportional to their corresponding optical depth. Increasing local time (given in degrees) indicates the ring particle motion (counterclockwise). The Sun is assumed to be on the left so that the black lines on Saturn and the rings correspond to Saturn's terminator and shadow edges ($\cos \Theta_s = \sqrt{(1 - (R_e/R)^2)(1 + \tan(B'R_e/R_p)^2)}$, with $B' = -21°.2$ (scan a), $R_p = 54\,508$ km, and $R_e = 60\,330$ km, see also Pilorz et al. 2015).
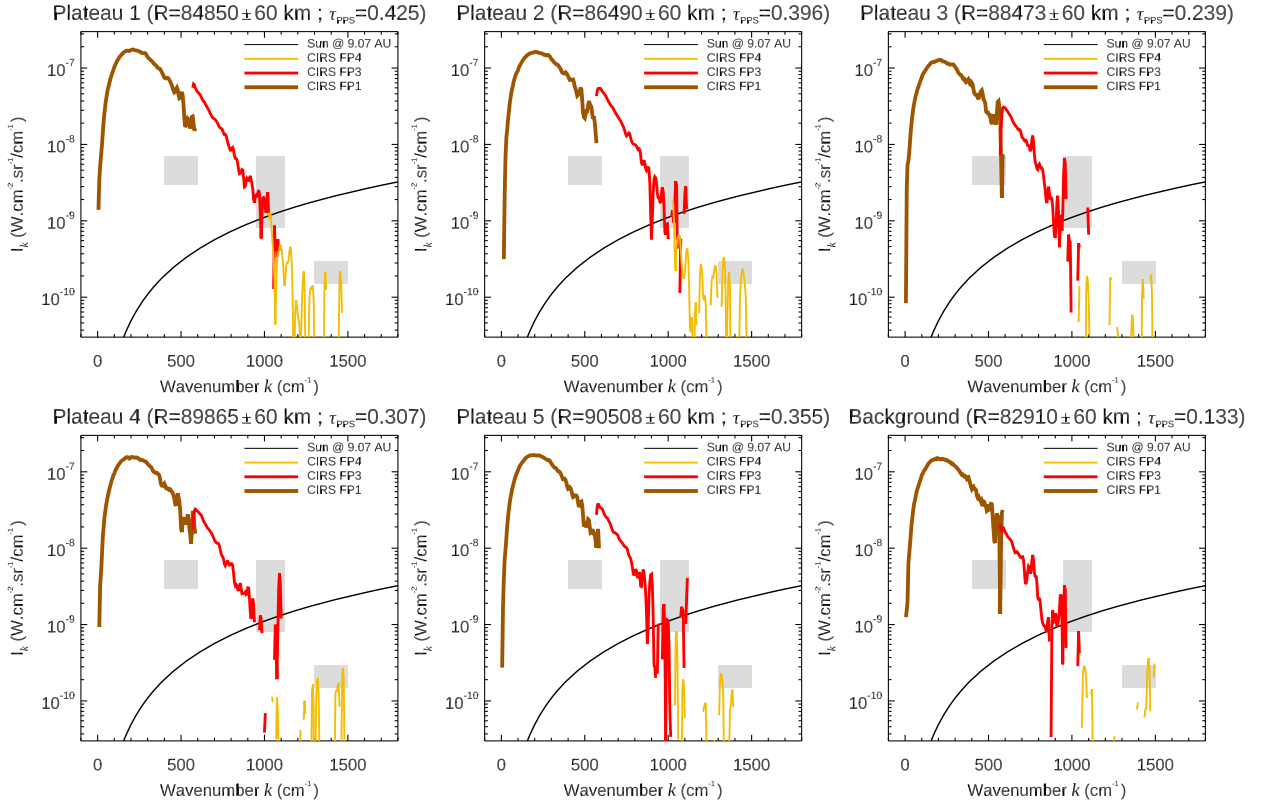

Figure 4. Spectrogram of one of the *four original* observations (scan a, aka 0PHASE001 during Rev 10) where the FP1, FP3, and FP4 scans are shown in image format as functions of ring plane radius and wavelength. Violet to red colours indicate increasing levels of IR brightness I_k for each focal plane: FP1: [7.44 × 10^{-13}, 2.07 × 10^{-07}] W cm^{-2} sr^{-1} cm^{-1}, FP3: [1.99 × 10^{-14}, 7.08 × 10^{-08}] W cm^{-2} sr^{-1} cm^{-1}, and FP4: [6.26 × 10^{-15}, 8.86 × 10^{-09}] W cm^{-2} sr^{-1} cm^{-1}.

ISS data that are also in brightness. The brightness at 636.94 cm^{-1} (or 15.7 μm, see Fig. 5) is representative of the IR brightness. Moreover, the signal is smooth, and there are no sharp features as observed at shorter wavelengths. We have then processed FP3 data in spectral radiance at 15.7 ± 0.2 μm, see Fig. 6. With scans a, b, c, and g, the plateaus are well resolved. With scan d, the signal is noisy, and only a few peaks can be discerned above the noise.

A closer look at the plateaus' shape from the FP3 signal in Fig. 6 shows that the plateaus' sharp edges are not resolved with FP3 because they are convolved with the surrounding background, which means that the typical shape of the plateaus with FP3 is similar to a Gaussian curve. This is why we did not use the range method of Altobelli et al. (2007), which consists in selecting only the FP3 footprints that are inside the plateau region. Indeed, without sharp edges, and with a Gaussian radial profile, the range method produces a lower averaged radiance, and a large standard deviation, even by selecting signal over a radial range smaller than the plateaus' width (e.g. ±60 km, see regions highlighted in grey in Fig. 6). Instead, we fit the plateau radial profile by a Gaussian function:

$$I_k(R) = G_0 e^{-(R-G_1)^2/2G_2^2} + G_3 + G_4 \cdot R + G_5 \cdot R^2, \qquad (9)$$

where G_0 to G_5 are coefficients, and R is the radial distance from Saturn. Best fits are shown in Fig. 6. Note that we have separated scan a in 10 distinct radial profiles in Fig. 6, one for each of the 10 FP3 pixels. This was to take advantage of the phase angle coverage of this scan.

As seen in Fig. 6, the agreement between the FP3 data and the Gaussian function is very good. In scan a at higher phase angle, where the scan is incomplete for the two inner plateaus, the fit is somewhat less good, and the Gaussian fits provide wider plateau profiles. Morishima et al. (2017) attributed this behaviour to navigation inaccuracy that seemed impossible to correct with a simple radial offset. Indeed, for most of the radial profiles, there can be a navigation inaccuracy that leads to radial offset of less than 50 km. Note that for this particular scan, some footprints appear to be inside Saturn's shadow (Fig. 3), however, considering the navigation inaccuracy, it is likely that they are not. Still, if they were, the shadowed footprints would not bias our results, because only the peak of the Gaussian curve is retained and used to build the CIRS brightness opposition phase curves.

Because the CIRS data have a poor phase sampling (a dozen points over 40° of phase angle!), our attempts to fit the data with the linear-exponential model ($I_k(\alpha) = b_0 + b_1 \exp(-\alpha/2b_2) + b_3\alpha$, with b_0–b_3 parameters) fail to provide meaningful fits (see Fig. 7).

Figure 5. CIRS spectra recorded by the three focal planes FP1, FP3, and FP4 for one of the *four original* observations (scan a, aka 0PHASE001 during Rev 10). The spectra were taken at a spectral resolution of 16.5 cm^{-1}. Spikes in FP4, FP3, and FP1 are interferences from RTI noise. The extreme edges of each spectra have been removed because of the noise. Grey regions represent the NESR. The *Planck* function of the Sun at Saturn's heliocentric distance is also plotted as an indication of the expected level of solar reflected brightness measured by FP4. Missing FP3 and FP4 data correspond to negative values of I_k. About two dozen spectra were selected for each focal plane and averaged by ring region.

Indeed, for most of the plateaus, we obtain very small surge widths, and null linear slopes at larger phase angles, meaning that the phase curve is fully controlled by the exponential part. Moreover, we also obtain poor fits with the logarithmic model:

$$I_k(\alpha) = a_0 + a_1 \ln \alpha, \qquad (10)$$

especially for plateau 2, see Fig. 7, indicating that the behaviour of the thermal phase curves is far from being logarithmic, contrary to the optical phase curves (Fig. 2). Consequently, we use the linear model with $\alpha_1 = 5°$ and $\alpha_2 = 7°$:

$$I_k(\alpha < \alpha_1) = -A_0 \cdot \alpha + B_0, \qquad (11)$$

$$I_k(\alpha > \alpha_2) = -A_1 \cdot \alpha + B_1. \qquad (12)$$

Then, we use equation (5) to derive the morphological parameters of the surge from the outputs of the linear fit.

The values of the morphological parameters of the surge A and HWHM are given in the right-hand panel of Fig. 7. However, because of the poor α-sampling of the CIRS data, the only HWHM provided with the highest confidence is the one for plateau 1 (or P5) and only this value is retained for analysis and discussion in the rest of the paper. By contrast, because the amplitude is determined with a higher level of confidence, even with this data set (because we have values at the smallest phase angle possible, see also details in Déau 2007), amplitude values of all 6 ROIs will be kept for comparisons with ISS.

2.3 Comparison of CIRS and ISS FOVs

We have explained the impact of the different boresight for the CIRS spectrometers, now we want to compare ISS and CIRS FOVs and we know that the boresight will intervene here as well.
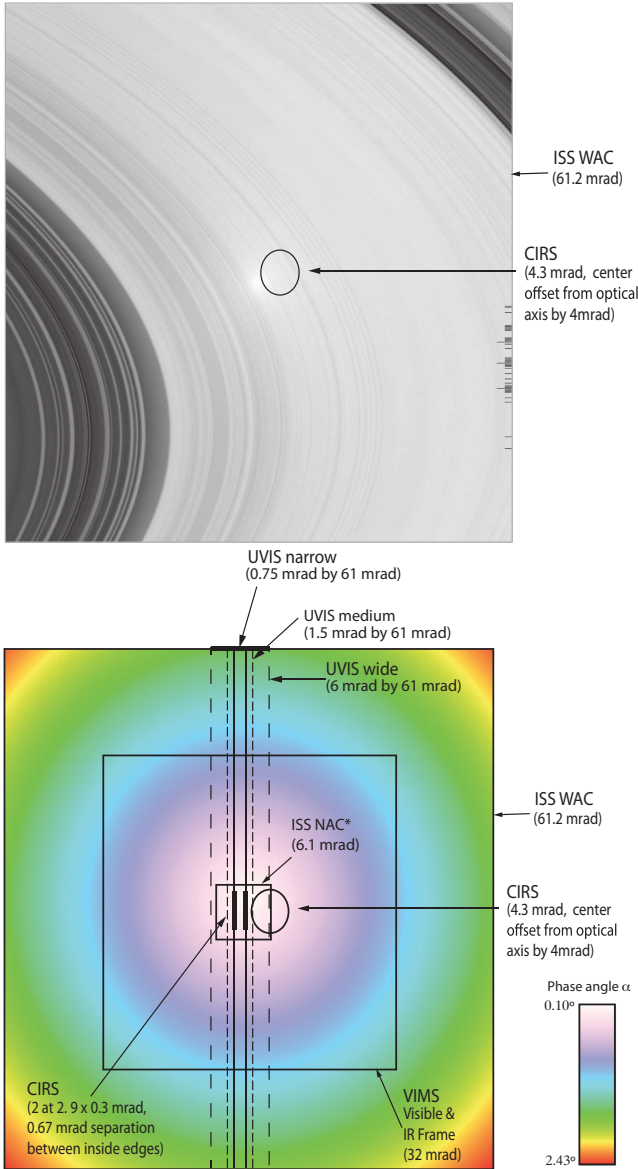
As shown in Fig. 8, FP1 has an offset of 4 mrad from the *x*-axis, while FP3 and FP4 have an offset of only 0.29 mrad. This is particularly important in scan a (CIRS_010RI_0PHASE001_VIMS) because this observation was requested by the VIMS (Visual and Infrared Mapping Spectrometer) team, and they designed this observation in such a way that the opposition spot was exactly at the centre of the VIMS frame. For ISS, who was riding this observation, the opposition spot is also at the centre of the WAC frame (see Fig. 8), because the NAC and WAC boresights are similar to that of the VIMS spectrometers. However, for CIRS, it means that FP1's footprint is not centred on the opposition spot, and misses the smallest phase angles. For FP3 and FP4, the 0.29 mrad offset is small enough to not create a large discrepancy in phase angles. Therefore, FP1 misses the highest radiance values corresponding to the smallest phase angles. As a result, scan a is critical in the C ring for FP1 because the lower radial resolution and the shifted angular FOV of FP1 are significant, meaning that any plateaus and narrow opposition spot are respectively spatial and geometrical features that are too small to be observed by FP1. Thus, to compare CIRS with ISS, only FP3 data are relevant.
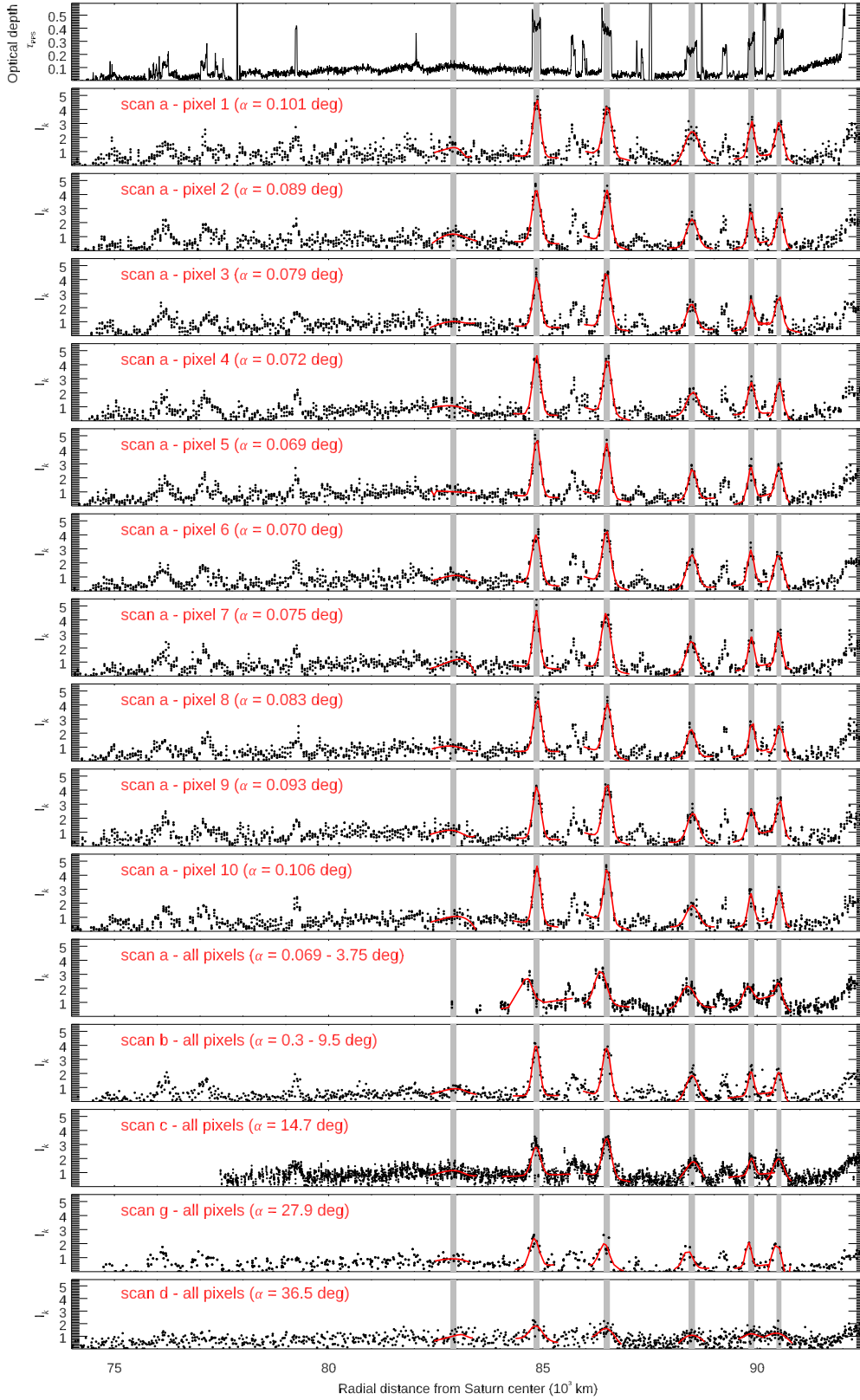
Figure 6. CIRS FP3 spectral radiance profiles (I_k in 10^{-8} W cm^{-2} sr^{-1} cm^{-1}) at 15.7 μm or 636.94 cm^{-1} of the *four original* scans (both portions of scan a represented separately: on top, the first portion at the lowest α separated per pixel, followed by the second portion at higher phase presented with all FP3 pixels grouped together). The geometry of all the scans is given in Fig. 3. The Voyager PPS optical depth in the top panel is given as a radial reference (Lane et al. 1982; Nicholson, Cooke & Pelton 1990). All scans were radially corrected from navigation inaccuracy. A level correction was applied to scan g to account for its lower $|B|$ compared to the *four original* scans. The six ROIs are highlighted in grey, and fit with the Gaussian function (solid line) seen in equation (9) to derive the spectral radiance's peak.
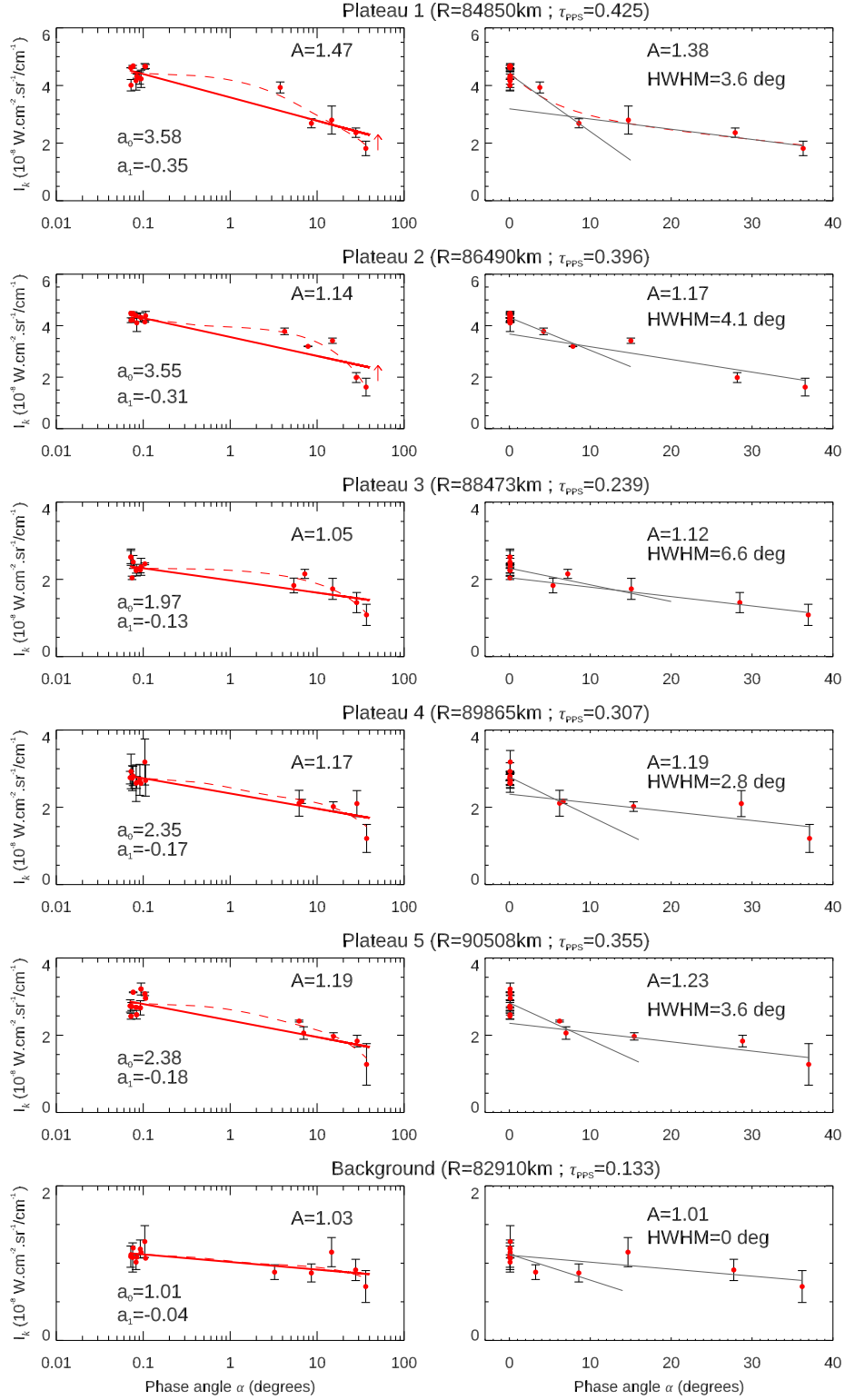
Figure 7. CIRS FP3 IR brightness I_k versus α curves derived for the same regions as Fig. 2. The IR brightness was extracted from the spectra using the *Gaussian method*. On the left, the data points are fit with the logarithmic function seen in equation (10, solid line), and the linear-exponential function given by $I_k(\alpha) = b_0 + b_1 \exp(-\alpha/2b_2) + b_3\alpha$ (dashed curve). The surge amplitude from this latter function ($A = (b_0 + b_1)/b_0$) is provided. The arrows in plateau 1 and 2's panel indicate the discrepancy of I_k values at high phase (scan d) predicted by the logarithmic and linear-exponential models. On the right, the data points are fit with the linear function seen in equations (11) and (12) (the set of two solid lines). The morphological parameters of the surge (A and HWHM) derived from the linear model are provided on the right. The linear-exponential function best fit (dashed curve) is plotted only for plateau 1, which is the only case where the fit led to similar width than the linear model (HWHM$=2b_2\ln 2 = 3°\!.8$). Note that while the linear-exponential fits of plateaus 2, 3, 4, and 5 seem acceptable on the left-hand panel, they are not reported on the right because they predict very narrow surges (e.g. for plateau 2, HWHM$=2b_2\ln 2 = 0°\!.08$) that we dismiss because they disagree with the values found with the linear model [e.g. for plateau 2, HWHM $= 4°\!.1$ with equation (5)].

logarithmic model used by Altobelli et al. (2007) tends to provide curves with a narrow surge and a shallow slope. For this model, we found very small values of HWHM (which were not calculated by Altobelli et al. 2007): less than 1°, see Figs B3–B5. By contrast, Altobelli et al. (2009) used a linear-exponential model, which provides various types of curves, but tends to provide large peaks with steep slopes. For this model, Altobelli et al. (2009) found HWHM values as large as 30° in the C ring, see their table 1, which is consistent with on own calculations using the same model (Fig. B6). This means that any tested morphological model other than the linear-logarithmic model would have provided a narrow surge (HWHM $\sim 4°$, see Fig. 7), but not extremely narrow as 0°.1. This result is quite significant because the widths discrepancy between the studies of Altobelli et al. (2007, 2009) is about two orders of magnitude, and if we use the linear model instead of the linear-logarithmic model, the discrepancy drops to one order of magnitude. For simplicity and from now on, the surge found with the linear-logarithmic model (Figs B3–B5) will be called the *narrow surge*. The surge derived from the linear model (Fig. 7) will be called the *intermediate surge*. Finally, the surge derived with the linear-exponential model (Fig. B6) will be called the *broad surge*, see Table 4.

(ii) *The phase angle sampling.* Because the phase angle sampling of the CIRS data set is very mediocre, morphological models tend to extrapolate between the points that are missing. For example, with our own phase curves in I_k (see Fig. 7), the linear model provides an angular width HWHM $\sim 4°$, whereas the linear-logarithmic model provides a significantly smaller width (HWHM $\sim 0°.1$, see Figs B3–B5). This is because there is no data between the zero phase point and the next point at 3°. More points in this area would have made all the different morphological models converge towards the same width values, as for the ISS data.

(iii) *The phase angle coverage.* In the study of Altobelli et al. (2007), the maximum phase angle is about 40°, whereas in the study of Altobelli et al. (2009), the maximum phase angle is 150°. Intuitively, it seems reasonable to expect a larger surge with the data that cover a larger range of phase angle.

(iv) *The focal planes.* Altobelli et al. (2007) used FP3 data, whereas Altobelli et al. (2009) used FP1 data. As this point has been discussed in the previous section, we refer the reader to the differences between the two focal planes in Section 2.2.

All in all, we can say that the use of various morphological models on various CIRS data sets was necessary to understand the discrepancies between the width values from Altobelli et al. (2007, 2009). In the following, our study will focus on the surge amplitude.

3.2 Results for CIRS FP1 and FP3 data

Now, we present the morphological results using various morphological models. We first start with the morphology of the thermal surge obtained with CIRS data, and we will finish with a comparison of the thermal and optical surges between themselves, and with microscopic and macroscopic ring signatures.

Previous work on the thermal surge morphology by Altobelli et al. (2007, fig. 12) did not find any trend between the narrow thermal surge of the plateaus and the optical depth. Recently, this result has been put to question by Déau et al. (2012), as the logarithmic fit to the CIRS FP3 data was questionable. Indeed, in half of the cases (plateaus 1, 4, and 5), a simple linear model would give a better fit than the logarithmic model (see Fig. B3). Therefore, the correlation

Figure 8. Top: FOV of a typical CIRS FP1 footprint projected over the FOV of an ISS Image (W1498453136) belonging to the 0PHASE001 observation corresponding to CIRS' scan a. The consequence of the 4 mrad offset of FP1 is illustrated by the misalignment of FP1 on the opposition spot, which was requested to be at the centre of the VIMS and ISS FOVs. The image contrast is slightly enhanced to make the opposition spot even more visible. Bottom: phase angle map of the same image (W1498453136) where colours indicate the phase angle. The FOVs of each instrument (ISS, CIRS, VIMS, and UVIS) are indicated. Adapted from Porco et al. (2004).

3 RESULTS

3.1 Narrow surge versus broad surge

One puzzle from previous CIRS studies is the discrepancy between the narrow surge found by Altobelli et al. (2007) and the broad surge found by Altobelli et al. (2009). There are several ways to understand why these two studies did not provide the same values for the thermal surge width.

(i) *The morphological models used.* Both studies used two different models that provide two different families of curves. The

Table 4. Summary of the morphological parametrization of the thermal opposition related to the angular width. Minimum radial and angular resolutions are given for scan a.

Surge type	Narrow surge	Intermediate surge	Broad surge
Reference	Altobelli et al. (2007)	This study	Altobelli et al. (2009)
HWHM	$<1°$	$\sim 4°$	$>30°$
α-range	$0°069$–$36°5$	$0°069$–$36°5$	$0°2$–$164°$
Focal plane	FP3	FP3	FP1
Minimum radial pixel size	164.4 km	164.4 km	1611 km
Minimum phase pixel size	$0°006$	$0°006$	$0°4$
Phase curve y-units	$T(K)$	I_k (W cm^{-2} sr^{-1} cm^{-1})	$T(K)$
Radial extraction	Range method	Gaussian method	Range method
Model used	Linear logarithmic	Linear	Linear exponential
Ref. figures	Fig. B3	Linear exponential Fig. 7	Fig. B6

between the thermal surge amplitude of the plateaus and the optical depth remains elusive. Our goal is to resolve this issue.

In the following, we will use several amplitudes from various morphological models. Note that we will not compare the values of these amplitudes directly, but rather their variations with the optical depth. Indeed, the absolute variations from each method depends on the data set used (either temperature of IR brightness), and on the morphological model. For the first case, we wanted to provide an analysis between the amplitudes of Altobelli et al. (2007, 2009), as we just done it in the previous section for the angular width. To do so, we fit the FP1 temperature data with a linear-exponential model (Fig. B6) and the FP3 temperature data of Altobelli et al. (2007) with a linear-logarithmic model (Fig. B3), as the reference studies. For the first data set, there is no clear trend with the optical depth, see Fig. 9, while in the second case, a correlation between A and τ appears only when plateau 2 is put aside.

We then revisited the study of Altobelli et al. (2007) by expanding their methodology:

(i) by working on IR brightness (or radiance I_k) rather than temperature to avoid assumptions on the blackbody fit and provide a coherent comparison between CIRS and ISS (i.e. by comparing brightness quantities);

(ii) by adding two additional data points to FP3 phase curves with scan g and the other portion of scan a (see Figs 3 and 6);

(iii) by applying the Gaussian method to extract the signal at the middle of the plateaus' location;

(iv) by using a morphological parametrization suited for the phase angle sampling and coverage of the phase curves.

The result of this new method tends toward a correlation between the thermal surge amplitude A of the plateaus and the optical depth, but now with the exception of plateaus 1 and 2. Indeed, as seen in Fig. 9, we have plotted a linear correlation between A and τ from plateaus 3–5, and it turns out that plateaus 1 and 2 deviate significantly from the values expected from that simple linear correlation. The discrepancy between the actual values of plateaus 1 and 2 and the expected values from the A–τ correlation is indicated in Fig. 9 by two arrows. What is the cause of this discrepancy? To look for an explanation of the marginal behaviour of plateaus 1 and 2 with our method using I_k with the Gaussian method, we have tried another method. We have used the range method of Altobelli et al. (2007) on the FP3 I_k data and we have used the linear-logarithmic model to fit the phase curves. Interestingly, in this case, we obtain a strong linear correlation between the surge amplitude and the optical depth for all the outer plateaus. A close inspection of the linear-logarithmic fit shows that the fit is poor at high phase for plateau

1 and for most phases for plateau 2, leading to a slope shallower than it actually is (see Fig. B4). This result also appears with the logarithmic fit of plateaus 1 and 2 seen in Fig. 7 that we previously noticed.

Therefore, the A–τ correlation is a strong trend for the last method tested (linear-logarithmic fit and range extraction method), but the poor fits of the morphological model for plateaus 1 and 2 is the reason for this strong linear correlation. This explains the discrepancy obtained earlier for plateau 2. The amplitude being a ratio between the y-intercept of two linear functions (one at low phase and one at higher phase), if the slope at higher phase is steep, it will *de facto* reduces the value of the amplitude. Interestingly, we notice from Fig. 7 that plateau 2 has a very steep slope at high phase compared to its logarithmic trend. We will seek the origin of steep slopes in the discussion.

All in all, we can conclude that: (1) the brightness at $0°$ is correlated to τ, however, the ratio of this brightness over the background intensity (which is basically the amplitude) is less correlated to τ and (2) the amplitude is not strongly correlated to τ in the outer C ring because of plateaus 1 and 2.

3.3 UVIS and VIMS micro- and macroproperties

We continue the analysis of the morphological parameters with some cross-correlations between the micro- and macroring signatures and the optical depth. The goal here is to see if the optical depth can be considered as a proxy for the other signatures. Our results are presented in Appendix A, in the right-hand panels of: Fig. A1 for the UVIS (UltraViolet Imaging Spectrograph) slope of $\tau_{uv} = f(|B_*|)$, Fig. A5 for the VIMS water ice band depths at 1.25, 1.5, and 2.0 μm, Fig. A6 for the VIMS spectral slopes S_{UV-B}^λ and S_{R-IR}^λ, and Fig. A9(a) for the ISS spectral slopes $|S_{VIO-BL}|$ and $|S_{RED-IR}|$. We do not notice any strong correlation between the optical depth and the microscopic signatures mentioned above (i.e. $BD_{1.25\,\mu m}$, $BD_{1.5\,\mu m}$, $BD_{2.0\,\mu m}$, S_{UV-B}^λ, S_{R-IR}^λ, $|S_{VIO-BL}|$, and $|S_{RED-IR}|$). This reinforces the intrinsic nature of these properties, as we consider the optical depth to be a macroscopic signature. Only the slope of $\tau_{uv} = f(|B_*|)$ is correlated with τ_{PPS} (Fig. A1), which indicates that the optical depth is strongly affected by the elevation angle in the optically thickest regions of the C ring. So far, this was demonstrated for the optically thick A and B rings (Colwell et al. 2006, 2007), but not for the C ring. From the cross-correlation with τ_{PPS}, several significant trends have emerged among each group of microscopic signatures that we find interesting to report:
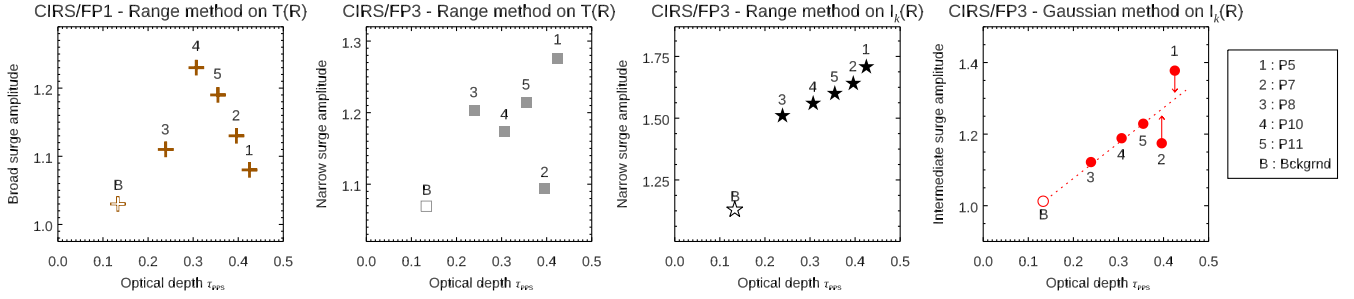
Figure 9. Comparison of the morphological parameters of the thermal surge with the optical depth τ_{PPS}. Different CIRS data sets and methods to extract the signal have been used to derive the amplitude of the surge, from left to right: CIRS FP1 temperature data with the range method (Fig. B6), CIRS FP3 temperature data with the range method (Fig. B3), CIRS FP3 radiance data with the range method (Fig. B4), and CIRS FP3 radiance data with the Gaussian method (Fig. 7). The arrows in the last panel indicate the discrepancy between the actual amplitude values of plateaus 1 and 2 and the expected values from a simple linear $A - \tau$ correlation from plateaus 3–5. Labels corresponds to the plateau number used by Altobelli et al. (2007) [alternate names by Colwell et al. 2009a are also provided in the legend on the right]. Note that when the calculated angular width is about $20°$, the peak is considered *broad*, when HWHM $<1°$, the peak is *narrow*, and finally, when HWHM $\sim 4°$, the peak is *intermediate*, see also Table 4.

(i) While the water ice band depths at 1.5 and 2.0 µm have the same non-monotonic trend with τ_{PPS}, the behaviour of $BD_{1.25\,\mu m}$ differs (Fig. A5). We note, however, that $BD_{1.25\,\mu m}$ is usually noisier (Filacchione et al. 2012; Hedman et al. 2013). As a consequence, further interpretation of these differences should be irrelevant;

(ii) The variations of VIMS' blue and red slopes with τ_{PPS} are perfectly opposite (Fig. A6), meaning that an increase of the red slope (S_{R-IR}^{λ}) with the optical depth corresponds to a decrease of the blue slope (S_{UV-B}^{λ}). In addition, when comparing Fig. A6 with Fig. A5, we note that the variations of S_{UV-B}^{λ} with the optical depth are very similar to those of $BD_{1.5\,\mu m}$ and $BD_{2.0\,\mu m}$;

(iii) The variations of the blue spectral slope $|S_{VIO-BL}|$ from ISS data with τ_{PPS} strongly differ at low and high phases when the phase angle is respectively $\alpha = 1°36$ and $92°23$ (Fig. A9a), while the variations of the red spectral slope $|S_{R-IR}|$ remain unchanged with α (Fig. A9b). Particularly, we note that the variations of $|S_{VIO-BL}|$ with τ_{PPS} at mid-phase are very similar to those of the VIMS blue slope (compare Figs A6 and A9a). Considering that the VIMS observations are also at moderate phase ($\alpha = 12°7$–$41°1$), we conclude that there is a total compatibility of the blue slope from ISS and VIMS data, and that the blue spectral slope does not vary with τ_{PPS} from phase angles of $12°7$ to $91°2$. However, the blue spectral slope varies significantly at low phase angle.

3.4 Comparisons of CIRS and ISS surges

We now proceed with a comparison of the morphological parameters of CIRS thermal surge (from FP3 I_k data, radially extracted with the Gaussian method) and ISS optical surge.

For the angular width (Figs 2 and 7), it appears that the surge width from CIRS FP3 ($HWHM_{CIRS} \sim 4°$) is about 10 times larger than the optical surge's width ($HWHM_{ISS} \sim 0°3$). CIRS data do not have enough phase angle sampling to allow an study of its HWHM radial variations.

For the amplitude, we can analyse its variations from plateau to plateau because this parameter was derived with a high confidence from two models (Fig. 7). Both CIRS and ISS are represented as a function of the distance to Saturn in Fig. 10. The variations with distance to Saturn show distinct patterns for the optical and thermal surge morphology. They appear to be monotonic for the optical

surge, while they are clearly non-monotonic for the thermal surge. This result will be interpreted in the next section.

3.5 Comparisons of CIRS, ISS, UVIS, and VIMS

Finally, we analyse the variations of the optical and thermal surge along with the main microscopic and macroscopic ring signatures. Among the various micro- and macrosignatures derived in Appendix A, we found that only $BD_{2.0\,\mu m}$ and τ_{uv} are strongly correlated with the optical and thermal surge morphologies, see Fig. 10. In particular, the optical surge is strongly anticorrelated with the water ice band depth, while the thermal surge is correlated with the optical depth, as they show similar variations with distance to Saturn, except for plateaus 1 and 2 (Fig. 10), as explained previously (Fig. 9). While we already noticed the positive correlation between the thermal surge morphology and τ_{uv} in Fig. 9, we note that the correlation appears a little bit clearer in Fig. 10. For the optical surge morphology, the strong correlation with $BD_{2.0\,\mu m}$ was also noticed by Déau et al. (2018), and is global in the C and B rings.

To summarize, the main results are the following:

(i) The thermal surge amplitude of the plateaus from CIRS FP1 data using the range method and seen in Fig. 9 are not exploitable because FP1 does not resolve the plateaus, and FP3 data in temperature miss the phase angle dependence due to the assumptions on the blackbody fit. This explains the previous inconclusive results of Altobelli et al. (2007).

(ii) The thermal surge amplitude (obtained with CIRS FP3 I_k data and the Gaussian method) is correlated with τ (Fig. 10), except for plateaus 1 and 2. This result is novel, and was possible to obtain due to the use of the Gaussian approach that allowed us to extract the signal with high fidelity, and a morphological parametrization suited for the phase angle sampling and coverage of the thermal phase curves.

(iii) The optical surge amplitude obtained with ISS data is correlated to the water ice band depth $BD_{2.0\,\mu m}$ (Fig. 10), as also reported in Déau et al. (2018).

(iv) None of the microscopic and macroscopic signatures seen in Appendix A other than τ_{uv} and $BD_{2.0\,\mu m}$ are correlated to the thermal and optical surge amplitudes, respectively.
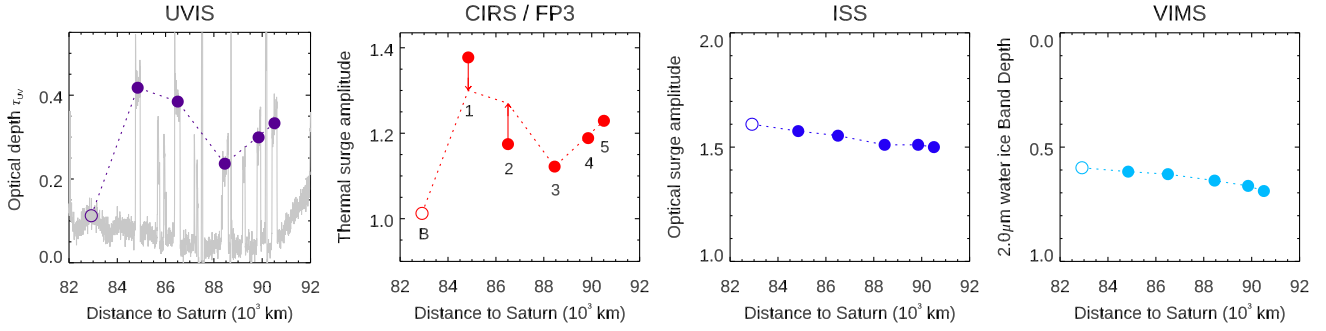
Figure 10. Variations of the thermal surge (CIRS FP3 I_k data with the Gaussian method at 15.7 μm or 636.94 cm^{-1}) and the optical surge (ISS I/F data at 0.6 μm) with the distance to Saturn for the six ROIs. The main micro- and macroscopic signatures of the rings (respectively, the water ice band depth at 2 μm from Filacchione et al. 2012, BD$_{2.0\,\mu m}$, and the optical depth, τ_{uv} from β-Cen occultation with $|B_*| = 66°72$) are also plotted for comparison purposes. The dotted lines just connect the points, except in the CIRS panel where the dotted line is designed to be similar to τ_{uv}. The arrows in the CIRS panel indicates the marginal behaviour of plateaus 1 and 2, also shown in Fig. 9. The legend is the same than in Fig. 9. Note that the y-axis of the VIMS panel is reversed.

We will interpret these results in terms of micro- and macroproperties, and opposition effect mechanisms in Section 4.

4 DISCUSSION

One limitation of the present approach is the phase sampling of the CIRS data, which prevented us from deriving morphological parameters other than A with a high degree of confidence with various morphological models. Indeed, because of the poor α-sampling of the CIRS data, the linear model was the only reliable option. However, without any point around 1° (see left-hand panel of Fig. 7), the retrieval of HWHM was more difficult with other models, except plateau 1, whose phase curve had a better α-sampling. We note however that even with more data, it is unlikely that the thermal phase curves would follow a logarithmic trend, and then exhibit a narrow surge, because the logarithmic model did not fit well the CIRS data (see Figs 7, B3, B4, and B5).

In Fig. 10, we have noticed strong deviations of the A–τ correlation due to plateaus 1 and 2. This result could suggest the action of another effect, and the ring roughness could be a good candidate. The C ring plateaus are actually known to be heterogeneous, with 100-m-sized holes called 'ghosts' created by 10-m-sized particles (Baillié et al. 2013), and non-propagating patterns called 'wavelike features' (Baillié et al. 2011). In Appendix A2, we have calculated a pixel entropy $\mathcal{H} = \sum_i \mathcal{P}_i \log_2(\mathcal{P}_i)$, see equation (A4), with masks of 5×5 and 10×10 pixels on a high-resolution ISS mosaic of the C ring (observation RDHRESCN001 from Rev 14). $\mathcal{H}$ quantifies the degree of detail contained in the images. We have found that $\mathcal{H}$ is strongly correlated to the number of wavelike features, and less with τ. In addition, plateau 2 has the highest pixel entropy and contains the most wavelike features, interestingly followed by plateau 1. Plateau 2 is, notably, the one whose behaviours deviate the most from the other plateaus (see Figs 9 and 10). As the roughness mostly affects the slope at higher phase (Lumme & Bowell 1981), the roughness created by wavelike features (or ring topography) could explain the discrepancies found in Figs 9 and 10, and also explain the distinct behaviours of plateaus 1 and 2 first reported by Altobelli et al. (2007). The ring topography will be studied in more detail in a subsequent work.

Finally, about the A–τ correlation found in the CIRS FP3 I_k data, the question then arises as to why this correlation exists. Is it because I_k is dependent on τ, via the scaling factor β? Indeed, the total IR flux is $\propto \beta T^4$, with T, the effective temperature, and β, a

factor scaling the *Planck* function at the level of the spectra, which theoretically depends on τ, see Appendix B3. We must say that $|B|$ is quite constant for the four original scans, and the amplitude being a brightness ratio, it should have washed out the τ-dependency. One clue would be to look at effective temperatures, since they are derived separately from β.

Two studies have derived FP3 temperatures for scan a (at $\alpha = 0°08$), and because FP3 spectra do not contain the *Planck* function's peak (see Fig. 5), assumptions on β were made by these studies to derive temperatures: for the first study, Altobelli et al. (2007), FP3 temperatures were obtained by a blackbody fit that assumed β from Voyager PPS τ, while for Morishima et al. (2017), FP3 temperatures resulted from a blackbody fit assuming β from Cassini UVIS τ.

We have plotted the temperatures of scan a from these two studies as a function of the generic optical depth in Fig. 11, with the IR brightness at 15.7 μm given as a reference. It appears that both the values and the τ-dependence of the plateau temperatures are different (see Fig. 11).

Discrepancies in temperature values are beyond the scope of this work, but will be studied in a future paper. On the other hand, the τ-dependence of plateau temperatures is interesting to discuss. Indeed, considering or not the τ-dependence of plateau temperatures yields different interpretations:

(i) If we do not consider the optical depth dependence of the plateau temperature as seen in Altobelli et al. (2007, fig. 12) and reported in Fig. 11, it means that the temperature could be related to ring particle surface properties such as: albedo, regolith texture, regolith thermal inertia Γ and IR emissivity ε_{IR}. So far, albedo derivations in the C ring (Cooke 1991) do not show radial variations similar to those of the temperatures of Altobelli et al. (2007). The other properties have not yet been derived with enough radial resolution to make conclusions. However, we note that none of the microscopic properties derived in Appendix A follow the trend of Altobelli et al. (2007, fig. 12).

(ii) If we do consider the optical depth dependence of the plateau temperature depicted in Fig. 11 from Morishima et al. (2017, fig. 5, left), it means that the temperature still contains the contribution of the ring layer (i.e. the collective effects of the ring particles). This would not be surprising since in the A ring, both effective temperature and scaling factor are affected by self-gravity wakes, e.g. Morishima, Spilker & Turner (2014). This generally leads to the idea that the effective temperature of heterogeneous rings is not the temperature of a single ring particle. Because most of
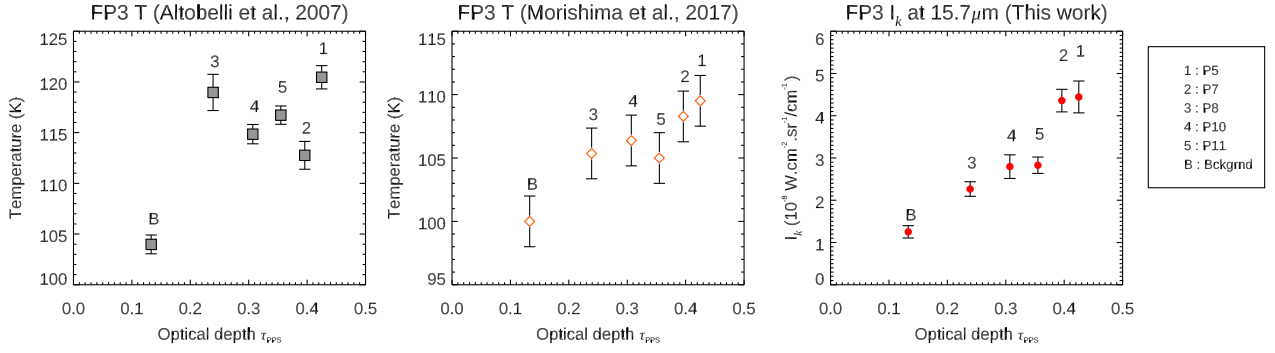
Figure 11. CIRS FP3 quantities of scan a for the six ROIs. Labels corresponds to the plateau number used by Altobelli et al. (2007) (alternate names by Colwell et al. 2009a are also provided in the legend on the right). The FP3 temperatures presented on the left-hand panel are from Altobelli et al. (2007, fig. 12) and are inferred from Voyager-PPS-based-β blackbody fit. The FP3 temperatures presented in the centre panel are from Morishima et al. (2017, fig. 5, left) and are inferred from Cassini-UVIS-based-β blackbody fit. On the right-hand panel, the IR brightness at 15.7 μm (I_k or spectral radiance) are from this study.

the plateau ring layer has wavelike features (Baillié et al. 2011) and large particles that create S-shaped features similar to the A ring's propellers (Baillié et al. 2013), the plateau ring layer is not homogeneous, and the effective temperature derived from a blackbody fit is not the temperature of a single ring particle. As a result, the optical depth dependence of plateau temperatures could be real, and could originate from the ring particle clumping instead of ring surface properties seen in the bullet detailed above.

However, we must note that blackbody fits using one parameter (only T) on FP3 data are limited, because the wavenumber range of FP3 does not cover the *Planck* function's peak. The absence of this peak in the FP3 spectra, and the assumptions on β ($\beta_{\text{therm}} = 1$, and $\varepsilon_{\text{IR}} = 1$, see Appendix B3) are very likely to shift the real effective temperature value to different solutions. If the τ-dependence of the plateau temperatures was to be maintained by new plateau-resolved FP1 data, it would confirm that the τ-dependence found here with FP3 I_k is not a simple scaling effect, but instead, the thermal behaviour of a heterogeneous ring.

5 CONCLUSIONS

In this study, we have used morphological models on Cassini's ISS and CIRS opposition data. This ISS/CIRS comparison was made possible by the use of FP3 data, which have the highest radial resolution and sensitivity among the CIRS spectrometers. We have found that the width of the surge seen by the two instruments is different: the thermal opposition surge (HWHM$_{\text{CIRS}} \sim 4°$) is about 10 times wider than the optical surge (HWHM$_{\text{ISS}} \sim 0°3$). Our conclusions are:

(1) We found that the C ring's thermal surge observed by Altobelli et al. (2007) is extremely narrow. Indeed, by using the linear-logarithmic model, which allows us to derive the surge morphological parameters from the logarithmic function used by Altobelli et al. (2007), we found HWHM<1°.

(2) By performing a benchmark of the morphological models on multiple CIRS data sets, our study suggests that the C ring's thermal opposition surge is not narrow (less than 1°) as seen with FP3 by Altobelli et al. (2007) nor broad (>30°) as seen with FP1 by Altobelli et al. (2009), but rather intermediate (with a width HWHM$_{\text{CIRS}} \sim 4°$ for plateau 1, also known as P5), see Table 4 for a summary. We think that the narrow surge obtained by Altobelli et al. (2007) was due to the narrow-surge-assumption made by the

logarithmic model when it interpolated the missing data. Moreover, while the narrow surge from Altobelli et al. (2007, see their fig. 9 and also Fig. B3) was not convincing for most of the plateaus, a medium-sized surge in IR brightness I_k appears here as a strong trend (see Fig. 7) because we have used a novel technique to extract the signal of the plateaus at their maximum, with the Gaussian method seen in equation (9). With a radial pixel size of ∼2000 km for scan a (which is the observation with the smallest phase angles reached by CIRS), it is clear that FP1 did not resolve the plateaus (see also Fig. B3). However, with a phase angle pixel size of 0°4, FP1 should have been able to resolve the thermal opposition surge of 4° seen by FP3. The reason why FP1 did not resolve the opposition surge in the plateaus is because each FP1 pixel contain not only the plateau's thermal signature, but also that of the surrounding background, and this background material does not exhibit an opposition surge (Fig. 7). On a side note, we conclude that there is no narrow surge in either FP3 or FP1 effective temperature data (see Figs B3, B5, and B6). The temperature behaviour with α is mostly linear (see Figs B3 and B5), which leads to the broad surge of several dozen degrees suggested by Altobelli et al. (2009). As a result, FP1 data should provide the 'linear' part of the phase curve, with the FP3–FP1 temperature difference representing the 'excess opposition surge' in the plateaus (see Figs B7 and B8).

(3) We confirm that the plateaus 1 and 2 are different in terms of thermal surge morphology (see Fig. 7), as previously claimed by Altobelli et al. (2007). These differences are due to their behaviour at larger phase (Fig. 7), as at low phase, their IR brightnesses are similar (Fig. 11).

(4) Differences between plateaus 1 and 2 can be explained when considering the wavelike features within these plateaus observed at high resolution using UVIS occultations (Baillié et al. 2011). In Table A3 of Appendix A, we have shown that the number of these features is directly correlated to the degree of detail contained in the images (that we have quantified with the pixel entropy, see Fig. A4). The correlation between the pixel entropy and the number of wavelike feature tends toward a large-scale roughness that can be called 'ring topography'. We will study this ring topography in a future work.

(5) The optical opposition effect of the C ring is not strongly correlated with the optical depth, in agreement with our previous study (Déau et al. 2013a). Since the optical opposition effect of the C ring is highly correlated with the water ice band depths (Fig. 9, see also Déau et al. 2018), we conclude that the nature of the optical ring

opposition effect in the C ring is mostly microscopic, and originates either from the grain size, the regolith porosity or the composition. In case of the grain size, the VIMS band depths lead to values from as small as 5 μm, see Fig. A7. For the composition, because no correlation has been found between the morphological parameters of the optical surge and the spectral slopes (Figs A6, A9a and b), the compounds that intervene in the spectral slopes (UV and spectrally neutral absorbers, see Hedman et al. 2013) are ruled out as the origin of the optical opposition effect. However, we note some significant changes in the ISS blue spectral slope near opposition compared to mid-phase (Fig. A9a), which are not observed with the ISS red slope (Figs A9b).

For the C ring's thermal opposition effect, because the surge amplitude is more correlated with τ (Fig. 9) than with any of the other microscopic and macroscopic signatures presented in Appendix A, we conclude that its nature is macroscopic.

Our work has highlighted significant temperature discrepancies between the focal planes of the CIRS instrument onboard Cassini. Our detailed analysis has brought new insights about CIRS capabilities and limitations for narrow or faint features. We summarize these findings in the following items:

(i) We have found that the behaviour of FP3 data above $\alpha > 30°$ taken at large distance to Saturn ($\sim 20 R_Y$) is noisy in the C ring. This remark is important to fully describe the thermal contrast between the plateaus and the background at moderate to high phase angle. While scan d shows very small thermal contrast (Fig. 6), we believe it should be similar to that of the other scans, but is below the sensitivity of the FP3 spectrometer when the spacecraft is at this distance. From the SOI data taken on the unlit side at high phase angle (when the spacecraft was very close to the planet, at $0.49 R_Y$), we have proof of a strong thermal contrast (~ 5 K) at high phase, see Altobelli et al. (2007, their fig. 5).

(ii) Blackbody fits using UVIS-based-β and PPS-based-β disagree on the optical depth dependence of the plateau temperatures (see Fig. 11). This dependence is present in the raw data (see Fig. 11, right), mostly because the IR brightness is still dependent on the scaling factor β (recall the total IR flux is $\propto \beta T^4$, see e.g. Pilorz et al. 2015), and β strongly depends on τ via the geometrical scaling factor β_{geom}, see equation (B21). If there is no τ-dependence in the plateau temperature, as claimed by Altobelli et al. (2007), then temperatures are assumed to be those of a single particle. If so, temperature variations observed at zero phase (Fig. 11, left and Altobelli et al. 2007, fig. 12) could be due to variations of albedo, texture of the regolith, thermal inertia Γ and/or IR emissivity $\varepsilon_{\mathrm{IR}}$ between particles of each plateau. Alternatively, if there is indeed a $T - \tau$ correlation in the plateau temperatures, as observed here (Fig. 11, centre, see also Spilker et al. 2006 for lit observations at much lower radial resolution), then we interpret it as an effect of the collective contribution of the ring particles, meaning that the temperature observed is still coupled to the clumping of the particles inside a ring patch. Considering that the azimuthal asymmetry in A ring temperatures is due to self-gravity wakes (Morishima et al. 2014), it is likely that the dynamical activity in the plateaus (propellers created by 10-m-sized boulders, see Baillié et al. 2013), and waves induced by resonances with satellites and mass anomalies inside the planet, see Table A3, Baillié et al. 2011; Hedman & Nicholson 2014) leads to temperature variations as well.

So far, FP3 blackbody fits using PPS or UVIS-based-β are inaccurate because the fits are performed on data that do not contain the

Planck function's peak. New plateau-resolved FP1 data obtained at the end of the Cassini mission, which contain the *Planck* function's peak, should lead to one of the two interpretations proposed.

REFERENCES

Altobelli N., Spilker L., Pilorz S., Brooks S., Edgington S., Wallis B., Flasar M., 2007, Icarus, 191, 691
Altobelli N., Spilker L. J., Leyrat C., Pilorz S., 2008, Planet. Space Sci., 56, 134
Altobelli N., Spilker L., Pilorz S., Leyrat C., Eddgington S., Wallis B., Flandes A., 2009, Geophys. Res. Lett., 36, 10105
Baillié K., Colwell J. E., Lissauer J. J., Esposito L. W., Sremčević M., 2011, Icarus, 216, 292
Baillié K., Colwell J. E., Esposito L. W., Lewis M. C., 2013, AJ, 145, 171
Balzter H., Tate N. J., Kaduk J., Harper D., Page S., Morrison R., Muskulus M., Jones P., 2015, Climate, 3, 227
Bobrov M. S., 1970, in Dollfus A.ed., Surfaces and Interiors of Planets and Satellites. Academic, New York, p. 376
Bradley E. T., Colwell J. E., Esposito L. W., 2013, Icarus, 225, 726
Brahic A., 1977, A&A, 54, 895
Brown R. H. et al., 2004, Space Sci. Rev., 115, 111
Carlson R. C., Guandique E. A., Jennings D. E., Pilorz S. H., Kunde V. G., 2009, in Advances in Imaging. Optical Society of America, p. FTuA5
Chandrasekhar S., 1960, Radiative Transfer. Dover, New York
Charnoz S., Porco C. C., Déau E., Brahic A., Spitale J. N., Bacques G., Baillie K., 2005, Science, 310, 1300
Clark R. N., Lucey P. G., 1984, J. Geophys. Res., 89, 6341
Clark R. N. et al., 2012, Icarus, 218, 831
Colwell J. E., Esposito L. W., Sremčević M., 2006, Geophys. Res. Lett., 33, 7201
Colwell J. E., Esposito L. W., Sremčević M., Stewart G. R., McClintock W. E., 2007, Icarus, 190, 127
Colwell J. E., Nicholson P. D., Tiscareno M. S., Murray C. D., French R. G., Marouf E. A., 2009a, The Structure of Saturn's Rings. Springer, Berlin, p. 375
Colwell J. E., Cooney J. H., Esposito L. W., Sremčević M., 2009b, Icarus, 200, 574
Colwell J. E., Esposito L. W., Jerousek R. G., Sremčević M., Pettis D., Bradley E. T., 2010, AJ, 140, 1569
Cooke M. L., 1991, PhD thesis, Cornell Univ., Ithaca, NY
Cuzzi J. N., Estrada P. R., 1998, Icarus, 132, 1
Cuzzi J. N., French R. G., Dones L., 2002, Icarus, 158, 199

Cuzzi J., Clark R., Filacchione G., French R., Johnson R., Marouf E., Spilker L., 2009, Ring Particle Composition and Size Distribution. Springer, Berlin, p. 459

Déau E., 2007, PhD thesis, Université Paris

Déau E., 2012, J. Quant. Spectrosc. Radiat. Transfer, 113, 1476

Déau E., 2015, Icarus, 253, 311

Déau E., Dones L., Rodriguez S., Charnoz S., Brahic A., 2009, Planet. Space Sci., 57, 1282

Déau E., Spilker L. J., Pilorz S., Brooks S., 2012, in AAS/Division for Planetary Sciences Meeting Abstracts. p. #501.02

Déau E., Dones L., Charnoz S., West R. A., Brahic A., Decriem J., Porco C. C., 2013a, Icarus, 226, 591

Déau E., Flandes A., Spilker L. J., 2013b, Icarus, 226, 1465

Déau E., Spilker L. J., Flandes A., 2016, Icarus, 272, 149

Déau E., Dones L., Mishchenko M. I., West R. A., Helfenstein P., Hedman M. M., Porco C. C., 2018, Icarus, 305, 324

Esposito L. W., Colwell J. E., McClintock W. E., 1998, Planet. Space Sci., 46, 1221

Esposito L. W. et al., 2004, Space Sci. Rev., 115, 299

Estrada P. R., Cuzzi J. N., Showalter M. R., 2003, Icarus, 166, 212

Filacchione G. et al., 2012, Icarus, 220, 1064

Filacchione G. et al., 2013, ApJ, 766, 76

Filacchione G. et al., 2014, Icarus, 241, 45

Flandes A., Spilker L., Morishima R., Pilorz S., Leyrat C., Altobelli N., Brooks S., Edgington S. G., 2010, Planet. Space Sci., 58, 1758

Flasar F. M. et al., 2004, Space Sci. Rev., 115, 169

French R. G., Verbiscer A., Salo H., McGhee C., Dones L., 2007, PASP, 119, 623

Hedman M. M., Nicholson P. D., 2014, MNRAS, 444, 1369

Hedman M. M., Stark C. C., 2015, ApJ, 811, 67

Hedman M. M., Nicholson P. D., Salo H., Wallis B. D., Buratti B. J., Baines K. H., Brown R. H., Clark R. N., 2007, AJ, 133, 2624

Hedman M. M., Nicholson P. D., Cuzzi J. N., Clark R. N., Filacchione G., Capaccioni F., Ciarniello M., 2013, Icarus, 223, 105

Jerousek R. G., Colwell J. E., Esposito L. W., Nicholson P. D., Hedman M. M., 2016, Icarus, 279, 36

Kaasalainen S., Muinonen K., Piironen J., 2001, J. Quant. Spectrosc. Radiat. Transfer, 70, 529

Kolokolova L., Liu L., Buratti B., Mishchenko M. I., 2011, J. Quant. Spectrosc. Radiat. Transfer, 112, 2175

Lane A. L. et al., 1982, Science, 215, 537

Leyrat C., Spilker L. J., Altobelli N., Pilorz S., Ferrari C., 2008, Planet. Space Sci., 56, 117

Lumme K., Bowell E., 1981, AJ, 86, 1705

Lumme K., Irvine W. M., 1976, AJ, 81, 865

Morishima R., Spilker L., Salo H., Ohtsuki K., Altobelli N., Pilorz S., 2010, Icarus, 210, 330

Morishima R., Spilker L., Turner N., 2014, Icarus, 228, 247

Morishima R., Turner N., Spilker L., 2017, Icarus, 295, 74

Nicholson P. D., Cooke M. L., Pelton E., 1990, AJ, 100, 1339

Nicholson P. D. et al., 2008, Icarus, 193, 182

Nicholson P. D., French R. G., Hedman M. M., 2016, in AAS/Division of Dynamical Astronomy Meeting. p. 400.03

Pilorz S., Altobelli N., Colwell J., Showalter M., 2015, Icarus, 254, 157

Porco C. C. et al., 2004, Space Sci. Rev., 115, 363

Porco C. C. et al., 2005, Science, 307, 1226

Porco C. C., Weiss J. W., Richardson D. C., Dones L., Quinn T., Throop H., 2008, AJ, 136, 2172

Poulet F., Cuzzi J. N., 2002, Icarus, 160, 350

Poulet F., Cuzzi J. N., French R. G., Dones L., 2002, Icarus, 158, 224

Poulet F., Cruikshank D. P., Cuzzi J. N., Roush T. L., French R. G., 2003, A&A, 412, 305

Rosen P. A., Tyler G. L., Marouf E. A., 1991a, Icarus, 93, 3

Rosen P. A., Tyler G. L., Marouf E. A., Lissauer J. J., 1991b, Icarus, 93, 25

Salo H., French R. G., 2010, Icarus, 210, 785

Salo H., Karjalainen R., French R. G., 2004, Icarus, 170, 70

Schmidt J., Ohtsuki K., Rappaport N., Salo H., Spahn F., 2009, Dynamics of Saturn's Dense Rings. Springer, Berlin p. 413

Shannon C. E., 1948, Bell Syst. Tech. J., 27, 379

Spilker L. J., Pilorz S. H., Edgington S. G., Wallis B. D., Brooks S. M., Pearl J. C., Flasar F. M., 2005, Earth Moon Planets, 96, 149

Spilker L. J. et al., 2006, Planet. Space Sci., 54, 1167

Spilker L., Ferrari C., Morishima R., 2013, Icarus, 226, 316

Spilker L. J., Ferrari C., Altobelli N., Pilorz S. H., Morishima R., 2018, Thermal Properties of Rings. Springer, Berlin, p. 399

Wallis B. D., Spilker L. J., Pilorz S. H., Pearl J. C., Altobelli N., Edgington S. G., Flasar F. M., 2005, AGU Meeting. p. B250

Wallis B. D., Pilorz S., Spilker L. J., Altobelli, 2006, in AAS/Division for Planetary Sciences Abstracts #38, p. 561

Zebker H. A., Marouf E. A., Tyler G. L., 1985, Icarus, 64, 531

SUPPORTING INFORMATION

Supplementary data are available at *MNRAS* online.

cring1_oe_cirs_iss_appendix.pdf

Please note: Oxford University Press is not responsible for the content or functionality of any supporting materials supplied by the authors. Any queries (other than missing material) should be directed to the corresponding author for the article.

This paper has been typeset from a TEX/LATEX file prepared by the author.